RESEARCH ARTICLE
MATERIALS SCIENCE

Size controllable single-crystalline Ni-rich cathode for high-energy lithium-ion batteries

Ji-Lei Shi[1,5,†], Hang Sheng[1,†], Xin-Hai Meng[1,5,†], Xu-Dong Zhang[1], Dan Lei[1], Xiaorui Sun[2], Hongyi Pan[2], Junyang Wang[2], Xiqian Yu[2,*], Chunsheng Wang[4,*], Yangxing Li[3,*] and Yu-Guo Guo[1,5,*]

[1]CAS Key Laboratory of Molecular Nanostructure and Nanotechnology, Beijing National Laboratory for Molecular Sciences (BNLMs), Institute of Chemistry, Chinese Academy of Sciences (CAS), Beijing 100190, China;

[2]Beijing Advanced Innovation Center for Materials Genome Engineering, Institute of Physics, CAS, Beijing 100190, China;

[3]Chery New Energy Automobile Co., Ltd, Wuhu 241002, China;

[4]Department of Chemical and Biomolecular Engineering, University of Maryland, College Park, MD 20742, USA;

[5]University of Chinese Academy of Sciences, Beijing 100049, China

[†]Equally contributed to this work.

***Corresponding authors.** E-mails: ygguo@iccas.ac.cn; xyu@iphy.ac.cn; cswang@umd.edu; liyangxing@mychery.com

ABSTRACT

Single-crystalline Ni-rich (SCNR) cathode with a large particle size can achieve a high energy density and safety over the polycrystalline counterparts. However, synthesis of large SCNR cathodes (>5 μm) without compromising electrochemical performance is very challenging due to incompatibility between Ni-rich cathodes and high temperature calcination. Herein, we introduce Vegard's Slope as a guidance to rationally select sintering aids, and successfully achieved size-controlled SCNR cathodes, the largest of which can be up to 10 μm. Comprehensive theoretical calculation and experimental characterization show that sintering aids continuously migrate to the particle surface, suppress sublattice oxygen release and reduce the typical exposed facets energy, which promote grain boundary migration and elevate calcination critical temperature. The dense SCNR cathodes fabricated by packing of different size SCNR achieve the highest electrode press density of 3.9 g cm^{-3} and a highest volumetric energy density of 3000 Wh L^{-1}. The pouch full cell demonstrates a high energy density of 303 Wh Kg^{-1}, 730 Wh L^{-1} and 76% capacity retention after 1200 cycles. SCNR cathodes with an optimized particle size distribution can meet the requirements for both EVs and portable devices. Furthermore, the principle for controlling the growth of SCNR particles can be widely applied to synthesize other materials for Li-ion, Na-ion and K-ion batteries.

Keywords: lithium-ion batteries, high energy density, Ni-rich cathodes, single-crystalline, surface energy

INTRODUCTION

Since the commercialization of lithium-ion batteries (LIBs) in the 1990s, $LiCoO_2$ has been considered as the first choice of cathode materials especially in 3C products (computers, communications and consumer electronics), for its highest volumetric energy density among commercially available cathode materials (Fig. S1a and b) (1-4). However, due to the scarce resources, high price and severe environmental pollution of cobalt, Ni-rich cathodes have attracted much attention as a more sustainable choice (5-8). Ni-rich cathodes have a high specific energy and cost-effectiveness, which are suitable for electric vehicles application (9-11). However, they fail to be applied in 3C due to lower volumetric energy density from a lower packing density compared to $LiCoO_2$ (Fig. S1c and d) (12-14).

Single crystallization is a smart strategy, which can improve not only safety by alleviating interface degradation but also the energy density via increasing electrode press density (15-18). However, the currently available single-crystalline Ni-rich cathodes have a typical particle size less than 4 μm, which make the press density unsatisfactory enough. To further improve the press density of the Ni-rich cathodes benchmarking $LiCoO_2$, large single crystal is necessary to fully reduce voids. Generally, increasing calcination temperature is the most common method to promote crystal growth, but it may incur oxygen escape from the host structure, the reduction of partial Ni^{3+} and consequent formation of the non-stoichiometric phase, which will ultimately deteriorate the electrochemical performances (19-22). Therefore, relatively

low calcination temperature (<800°C) is generally preferred to synthesize Ni-rich cathodes so that super-large single-crystalline Ni-rich cathodes are unavailable (20,23). Although the molten-salt-assisted method can be used to synthesize SCNR cathodes, it tends to induce impurity phases and needs an additional water washing process to remove the residual salt, which severely reduces the cycle stability of the materials (17,24,25). Furthermore, the large SCNR cathodes have a long-range ordered crystalline structure, which is likely to cause lattice collapse after a large amount of Li^+ are extracted, consequently reducing the materials rate capability and cycle stability (26). Thus, synthesis of large SCNR cathodes (>5 μm) is very challenging (27).

Here, we have successfully prepared a series of SCNR cathode materials with controllable particle sizes in a range of 0.5-10 μm by using trace amounts of sintering aids Al_2O_3 and CeO_2. The introduction of CeO_2 dramatically promotes the crystal growth by adjusting ion mobility and surface energy, which allows a larger particle size. Meanwhile, the spectroscopic and structural characterizations reveal that Ce^{4+} is enriched on the surface and Al^{3+} distributes homogeneously in the bulk, enhancing the lattice and interface stability synergistically. The as-prepared SCNR cathode exhibits excellent electrochemical performances, and its available high press density enables the 4 Ah pouch cell delivering impressive energy densities of 303 Wh kg^{-1} and 730 Wh L^{-1}, at a competing level with the state-of-the-art LIBs using $LiCoO_2$ cathode. Thus, the SCNR cathode is qualified as an alternate of $LiCoO_2$, which will be bound

to alleviate cobalt reliance, contributing to the development of sustainable LIBs.

RESULTS

Optimization of sintering aids to promote crystal growth

The crystal growth at relatively low calcination temperature can be regulated using sintering aids which can be rationalized via Vegard's Slope (28). The sintering aids that do not match the host will have a large absolute Vegard's Slope. They are difficult to incorporate into the host crystal lattice, leading to enrichment on the particle surface instead (29). Some concentrated dopants on the surface of the particles may reach a specific ratio and form a eutectic film with a melting point below that of the two pure substances. This thin film promotes interface atomic diffusion even below the melting point (30). In contrast, the ions that match with the host with a small absolute Vegard's Slope can be incorporated into the crystal lattice, which has less impact on the growth of SCNR cathodes. The cations with different Vegard's slopes were selected as sintering aids to synthesize the SCNR particles (Fig. 1a). The size deviation of the SCNR particles correlates well with Vegard's Slope difference and CeO_2 and Bi_2O_3 indeed promote crystal growth of SCNR cathodes (Fig. 1b and Fig. S2). Compared with Ce^{4+}, the low valence of Bi^{3+} cannot ameliorate the kinetic hindrance in the large SCNR cathode, leading to an inferior performance (Fig. S3). Finally, we chose CeO_2 to obtain SCNR cathodes, simultaneously adding Al_2O_3 for its well-known function of stabilizing cathode structure.

Crystal growth mechanism

To understand the critical role of sintering aids in promoting crystal growth, the TM-O bond energy and surface energy were calculated based on the typically exposed facets (003), (104) and (012) of Ni-rich cathode (31). In solid-state synthesis, the mass transfer for crystal growth is dominated by grain boundary migration and the rate V_B can be demonstrated via the equation as follows, which is the product of mobility M_B and driving force ΔP (20).

$$V_B = -M_B \Delta P$$

$$M_B = \frac{f_a a^4}{k_B T} \exp[\frac{-E_A}{R_g T}] \quad \Delta P = g\Delta\gamma(\frac{1}{G_1} - \frac{1}{G_2})$$

Where k_B and R_g are Boltzmann constant and gas constant, respectively. Besides the intrinsic atomic size a and vibration frequency f_a, temperature T and activation energy E_A account for a prominent influence on M_B with an Arrhenius relation, which means raising temperature can accelerate grain growth dramatically. Ce-O bonds have higher bond energy than Ni-O bonds in the above three facets (Fig. 1c and Fig. S4a), which can stabilize lattice oxygen atoms and suppress the release of oxygen from sublattice at a high temperature. Thus, the enhanced Ce-O bonds will allow a higher calcination temperature T for the cathodes with Ce^{4+} doping. On the other hand, the driving force ΔP lies in surface energy difference $\Delta\gamma$ and the discrepancy of sizes G_1, G_2 between adjacent grains. g is a geometric factor dependent on grain shape. Specifically, small grains are prone to coalesce into large grains so that surface energy

can be reduced due to a lower specific surface area, similar with Ostwald ripening. Ce^{4+}-doped SCNR cathodes show lower surface energy than those without Ce^{4+} doping in all three surfaces (Fig. 1d and Fig. S4b), so CeO_2 is thermodynamically favored on the surface of SCNR particles. The segregation of Ce^{4+} on the particle surface will further reduce the surface energy (namely increase $\Delta\gamma$), so Ce^{4+} will promote crystal growth to reach a thermodynamically stable state.

Structure of SCNR cathodes

By employing CeO_2 and Al_2O_3 as sintering aids, we synthesized SCNR cathode particles with sizes ranging from 500 nm to 10 μm by adjusting calcination temperature, and the crystal grains are smooth without visible residual alkali salts (Fig. 2a and b, and Fig. S5a-f). As shown in Fig. 2c and Table S1, we synthesized 10 μm SCNR cathode particles, which is the largest Ni-rich single-crystalline cathode reported to date. In addition, all SCNR cathode particles were prepared at the pilot scale (Fig. S5g and h). According to powder X-ray diffraction (XRD), SCNR cathode materials conform to the typical *R*-3*m* layered structure without any impurity phases. More specifically, the Rietveld refinement analysis for the XRD pattern of the large SCNR sample (10 μm) synthesized at 950°C yields lattice parameters of $a = b = 2.874$ Å, $c = 14.197$ Å with a Li/Ni cation mixing of 2.6% (Fig. 2d). Such a low level of cation mixing indicates a well-preserved layered structure at a calcination temperature of 950°C due to adding of sintering aids CeO_2 and Al_2O_3.

The crystal structure of 10 μm SCNR cathode at atomic scale was characterized

using spherical aberration-corrected scanning transmission electron microscope (STEM) imaging with focused ion beam (FIB) preparation (Fig. 2e). The cross-section image demonstrates that the bulk of the particle is dense without any void or crack (Fig. 2f). Atomic-resolution STEM results further verify the bulk layered structure without obvious cation-mixing (Fig. 2g), while a thin layer of rock-salt phase can be found on the particle surface (Fig. 2h), which may be attributed to the surface enrichment of Ce^{4+}.

To verify the promoting mechanism of crystal growth, nanoscale X-ray computed tomography (Nano-CT) was utilized to resolve the spatial distribution of the trace Ce^{4+} in two SCNR particles with different size of 3 μm and 10 μm. The process is shown in detail as Fig. S6. Both SCNR cathode materials are single-crystalline particles with a small amount of segregation phase shell on the particle surface. The segregation phase for the 10 μm particle is about twice the thickness of that for the 3 μm one (Fig. S7a). On the 3 μm particle, the surface segregation phase is sparsely distributed and locally enriched (Fig. 2i). However, a dense and well-connected surface segregation phase covers on the 10 μm particle (Fig. 2j). Statistically, the segregation phase on the 10 μm particle shell has a larger average volume and a wider volume distribution than those on the 3 μm particle, demonstrating its densely covered morphology (Fig. S7b and c). The different Ce^{4+} distribution in the SCNR particles of two sizes indicates an unambiguous atomic diffusion tendency in the sintering process. As the grain grows, Ce^{4+} ions continuously

migrate to the particle surface. Meanwhile, the gradually intensified surface Ce^{4+} enrichment further drives mass transfer for crystal growth under thermodynamic momentum, which validates the potential mechanism of the particle size growth.

Performances of SCNR cathodes

The electrochemical performances of SCNR cathode materials with varying grain sizes are evaluated using half-cells (Fig. S8a-e). While the initial charge capacity is almost the same (Fig. S8f), the specific discharge capacity decreases from 210 to 191 mAh g^{-1} as the particle size increases from 500 nm to 10 μm. This phenomenon indicates the poorer lithium diffusion kinetics for the larger SCNR particles, which is in agreement with the Fick's first law of diffusion ($\tau_{eq} \sim L^2/2D$, where τ_{eq} is diffusion time, D is diffusion coefficient, L is diffusion length) (32). When the charge-discharge rate is reduced to 0.01 C, the specific discharge capacity of 10 μm SCNR cathode is restored to 205 mAh g^{-1}, which is close to that of 500 nm cathode, suggesting that the capacity loss resulting from the sluggish reinsertion of Li^+ is reversible (Fig. S8g and h). We also make the comparison of the first charge-discharge curves of pristine single crystals, polycrystals, single crystals synthesized with different sintering aids (Fig. S9a-i). It can be seen that most modified single crystal samples exhibit similar capacity with the pristine ones.

Given that the large SCNR cathode is essential for increasing volumetric energy density, we then focused on testing 10 μm SCNR cathode in half-cells to evaluate its application potential for LIBs. The cathode delivers a high specific discharge capacity

of 191 and 200 mAh g^{-1} at 0.1C with a charging cut-off voltage of 4.3 and 4.5 V respectively (Fig. 3a). Meanwhile, there is negligible voltage polarization less than 0.01 V observed from the charge-discharge curves after 100 cycles at 1C, which can be attributed to the stable interface during repeated cycling (Fig. 3b). The SCNR cathode also demonstrates a good rate capability, preserving a discharge capacity of around 150 mAh g^{-1} even under a high rate of 5C (Fig. 3c). The exceptional cycling stability in the voltage range of 3-4.3 V with a capacity retention of 80.4% after 350 cycles is also demonstrated (Fig. 3e). When the charging cut-off voltage is increasd to 4.5 V, the capacity can still maintain 94.4% after 100 cycles (Fig. 3d).

The electrochemical performance of LIBs is closely related to the evolution of the cathode-electrolyte interphase (CEI) during cycling. *Ex-situ* X-ray photoelectron spectroscopy (XPS) and electrochemical impedance spectroscopy (EIS) are performed to reveal the CEI evolution process of SCNR cathodes. The evolution of F 1*s*, C 1*s*, and O 1*s* spectra for different cycles (Fig. S10) suggests that the CEI relevant components of LiF, C=O, C-O, and C-H increase distinctly before 20 cycles. Then there is only a slight increase of these CEI species in the subsequent cycles, confirming the stability of CEI. In terms of the electrode kinetics as shown in EIS (Fig. S11a), there is little change of charge-transfer resistance for the first 100 cycles, which also indicates that a stable CEI was formed on the cathode during cycling. This observation can be likely attributed to the beneficial Ce^{4+} enriched nanoscale rock-salt layer on the surface of the SCNR sample, which acts as a surface protective layer for

the cathode and stabilizes the CEI.

Thermal and structural stabilities of cathode materials are critical factors for battery safety, which is important for practical application. The 3 μm SCNR cathode sample is much more thermally stable compared to the reported agglomerated polycrystalline NCM811 with spherical particles. More importantly, when the particle size of SCNR cathode increases from 3 to 10 μm, the thermal decomposition temperature further increases from 280.8°C to 286.8°C, whilst the exothermic heat is reduced from 1463 J g^{-1} to 982.9 J g^{-1}, demonstrating a great benefit of designing large single-crystalline Ni-rich cathodes for safety enhancement of LIBs (Fig. S11b). The *in-situ* XRD results in Fig. S11c show excellent structural stability. The (003) peak gradually shifts to a lower angle with the increase of operating voltage, but it moves reversely to higher angle side when the charging voltage is higher than 4.1 V, suggesting that the lattice parameter *c* expands first but then drops during the Li^+ extraction process.

SCNR cathode was also evaluated in commercial pouch cells using commercial graphite or SiO_x/graphite anodes. To further improve electrode tapping density, we filled packing voids among large particles with smaller ones. For simplicity, we take face-centered cubic (FCC) stacking of spherical particles for example here. If the octahedral and tetrahedral voids in the model are filled with spherical particles of appropriate sizes, the space utilization can further increase from 74% to 81% (Fig. 4a). In practice, a high loading of active materials up to ~22 mg cm^{-2} (single-side ~ 4.5

mAh cm^{-2}) is achieved, and the electrodes can reach slightly variable press densities by adjusting roll design (Fig. S11d-g). A press density of 3.9 g cm^{-3} is achieved, which is much higher than that of the electrode made by commercial NCM cathode (3.4 g cm^{-3}) and is also close to that of $LiCoO_2$ cathode (4.1 g cm^{-3}). To the best of our knowledge, the press density of 3.9 g cm^{-3} is the highest one for reported NCM cathode materials. The cross-section images clearly demonstrate the difference of voids and cracks distribution in the two kinds of densely-packed electrodes (Fig. 4b and c).

Two types of pouch cells are assembled to evaluate the battery performances. The designed capacity of single pouch cell is 2.9 Ah (vs. graphite, press density 1.5 g cm^{-3}) and 4 Ah (vs. SiO_x & graphite, capacity 500 mAh g^{-1}, press density 1.6 g cm^{-3}). The 4 Ah pouch cell exhibits both high specific gravimetric energy density of 303 Wh kg^{-1} and high volumetric energy density of 730 Wh L^{-1} (based on all components of the pouch cell) (Fig. 4d and Table S2). The 2.9 Ah pouch cell exhibits a remarkable cycle stability with a capacity retention of 76% after 1200 cycles (Fig. 4e), which is comparable with that of the $LiCoO_2$-based commercialized Li-ion batteries. Furthermore, the SCNR pouch cell possesses an impressing low-temperature performance. Take the capacity at 1C with a cut-off voltage of 4.25 V in room temperature as a benchmark, the SCNR cell exhibits 88% and 83% capacity retention in -10°C and -20°C respectively, which are significantly higher than those of NCM811 and $LiCoO_2$ (Fig. 4f). The thermal runaway behavior of SCNR pouch cells is also

investigated. Taking NCM811 and $LiCoO_2$ cathodes for comparison, we employ accelerating rate calorimetry (ARC) with a standard process of heat-wait-seek to acquire the accurate thermal runaway behavior in pouch cells (Fig. 4g and h, and Table S3). The onset temperature (T_1, abnormal heat generation) and triggering temperature (T_2, tipping point of sharp temperature increase) of the SCNR pouch cell is 92°C and 157 °C respectively, which are higher than those of $LiCoO_2$ (72°C and 146°C) and NCM811(83°C and 136°C). The results suggest that the thermal stability of large SCNR cathodes is superior than those of both polycrystalline NCM and single-crystalline $LiCoO_2$.

DISCUSSION

The comprehensive battery performances of SCNR cathode are compared to the commercial polycrystalline NCM811 and $LiCoO_2$ in the form of Radar map (Fig. 5 and Tables S4-S6). Compared to NCM811, SCNR cathode exhibits particularly outstanding safety and energy density besides other almost overlapped performances. SCNR cathode owns a similar particle size with typical commercial polycrystalline NCM811, but the grain boundaries are eliminated. Therefore, the detrimental side reactions and gaps can be reduced due to the lower specific surface area. In contrast to $LiCoO_2$, both cathodes possess the dense characteristic of single crystal, so SCNR cathode is able to own nearly the same energy density and safety with $LiCoO_2$. The most prominent advantage is the cost competitiveness of SCNR cathode, which makes it very attractive to substitute $LiCoO_2$ in 3C applications, thereby relieving cobalt resource strain in the next century remarkably (6,33-35). We would like to remind in the end that there can still exist the intrinsic drawbacks of Ni-rich cathodes like charge heterogeneity and cracking, which will be prominent especially for operation in high temperature. When temperature rises, the ions can overcome reaction barrier easier,

causing much severer internal stress evolution, and the reaction rate between Ni^{4+} and electrolyte can be increased dramatically. The interplay among lattice and surface defects, charge heterogeneity and high temperature cycle stability is a frontier research topic that is worth systematic follow-up efforts.

In conclusion, it is not hard to acquire large-size single-crystalline Ni-rich cathodes, which can be achieved just only by elevating calcination temperature. However, the SCNR cathodes obtained in that way cannot own competitive electrochemical performance with polycrystalline counterparts and $LiCoO_2$. High temperature can endow ions enough mobility to overcome barriers between grain boundaries, but it comes at a cost to destroy layered structure with severe cation disordering. The adding of CeO_2 in this work accelerates the mass transfer along grain boundaries via a micro-liquid environment around grains and enhances surface energy drive, promoting crystal growth both kinetically and thermodynamically. Besides, Ce^{4+} ions segregate on the particle surface to construct a stubborn rock salt layer, and Al^{3+} is simultaneously incorporated into the bulk lattice, enhancing the layered structure. Benefited from the synergistic effect, SCNR cathode is able to successfully grow without disturbing electrochemical performance a lot. It is noteworthy that the selection of sintering aids is not unique, which can be further explored by referring to Vegard's Slope. Our findings provide the methodology to synthesize the large single-crystalline Ni-rich NCM cathode with superior battery performances, which are very promising to alleviate the sustainability issue related to cobalt resources.

FUNDING

This work was supported by CAS Project for Young Scientists in Basic Research (YSBR-058), the Basic Science Center Project of Natural Science Foundation of China (51788104), the National Natural Science Foundation of China (22222904 and 22179133), the 'Transformational Technologies for Clean Energy and Demonstration' Strategic Priority Research Program of the Chinese Academy of Sciences (XDA21070300). Ji-Lei Shi thanks the financial support from the Youth Innovation Promotion Association CAS (2019033).

AUTHOR CONTRIBUTIONS

Y.-G.G., Y.L, and J.-L.S. initiated this project and conceived the idea. J.-L.S., H.S., X.-D.Z., X.Y., X.-H.M. and Y.L carried out the experimental work, data collection and analysis. H.P., X.S., J.W. and X.Y. performed the Nano-CT, ARC measurement, first principles calculations and data analysis. J.-L.S., X.-D.Z., D.L. X.Y., Y.L conducted the pouch cells evaluation. J.-L.S., X.-H.M., X.Y., Y.L, C.W. and Y.-G.G. prepared this manuscript with contributions from all other authors.

Conflict of interest statement. None declared.

REFERENCES

1 Whittingham MS. Lithium batteries and cathode materials. *Chem Rev* 2004; **104**: 4271-301.

2 Li M, Lu J and Chen Z *et al*. 30 years of lithium-ion batteries. *Adv Mater* 2018; **30**: 1800561.

3 Dunn B, Kamath H and Tarascon JM. Electrical energy storage for the grid: a battery of choices. *Science* 2011; **334**: 928-35.

4 Armand M and Tarascon JM. Building better batteries. *Nature* 2008; **451**: 652-7.

5 Olivetti EA, Ceder G and Gaustad GG *et al.* Lithium-ion battery supply chain considerations: analysis of potential bottlenecks in critical metals. *Joule* 2017; **1**: 229-43.

6 Fu X, Beatty DN and Gaustad GG *et al.* Perspectives on cobalt supply through 2030 in the face of changing demand. *Environ Sci Technol* 2020; **54**: 2985-93.

7 Bianchini M, Roca-Ayats M, Hartmann P *et al.* There and back again-the journey of $LiNiO_2$ as a cathode active material. *Angew Chem Int Ed* 2019; **58**: 10434-58.

8 Wang X, Ding YL and Deng YP *et al.* Ni-rich/Co-poor layered cathode for automotive Li-ion batteries: promises and challenges. *Adv Energy Mater* 2020; **10**: 1903864.

9 Zeng X, Li M and Abd El-Hady D *et al.* Commercialization of lithium battery technologies for electric vehicles. *Adv Energy Mater* 2019; **9**: 1900161.
10 Li WD, Erickson EM and Manthiram A. High-nickel layered oxide cathodes for lithium-based automotive batteries. *Nat Energy* 2020; **5**: 26-34.
11 Park K-J, Hwang J-Y and Ryu H-H *et al.* Degradation mechanism of Ni-enriched NCA cathode for lithium batteries: are microcracks really critical? *ACS Energy Lett* 2019; **4**: 1394-400.
12 Zhang J-N, Li Q and Ouyang C *et al.* Trace doping of multiple elements enables stable battery cycling of $LiCoO_2$ at 4.6 V. *Nat Energy* 2019; **4**: 594-603.
13 Qian J, Liu L and Yang J *et al.* Electrochemical surface passivation of $LiCoO_2$ particles at ultrahigh voltage and its applications in lithium-based batteries. *Nat Commun* 2018; **9**: 4918.
14 Yan P, Zheng J and Liu J *et al.* Tailoring grain boundary structures and chemistry of Ni-rich layered cathodes for enhanced cycle stability of lithium-ion batteries. *Nat Energy* 2018; **3**: 600-5.
15 Liu Y, Harlow J and Dahn J. Microstructural observations of "single crystal" positive electrode materials before and after long term cycling by cross-section scanning electron microscopy. *J Electrochem Soc* 2020; **167**: 020512.
16 Li J, Cameron AR and Li H *et al.* Comparison of single crystal and polycrystalline $LiNi_{0.5}Mn_{0.3}Co_{0.2}O_2$ positive electrode materials for high voltage Li-ion cells. *J Electrochem Soc* 2017; **164**: A1534-44.
17 Kim J, Lee H and Cha H *et al.* Prospect and reality of Ni-rich cathode for commercialization. *Adv Energy Mater* 2018; **8**: 1702028.
18 Cao Y, Li M and Lu J *et al.* Bridging the academic and industrial metrics for next-generation practical batteries. *Nat Nanotechnol* 2019; **14**: 200-7.
19 Kim UH, Jun DW and Park KJ *et al.* Pushing the limit of layered transition metal oxide cathodes for high-energy density rechargeable Li-ion batteries. *Energy Environ Sci* 2018; **11**: 1271-79.
20 Langdon J and Manthiram A. A perspective on single-crystal layered oxide cathodes for lithium-ion batteries. *Energy Storage Mater* 2021; **37**: 143-60.
21 Lee S, Jin W and Kim SH *et al.* Oxygen vacancy diffusion and condensation in lithium-ion battery cathode materials. *Angew Chem Int Ed* 2019; **58**: 10478-85.
22 Li W, Asl HY and Xie Q *et al.* Collapse of $LiNi_{1-x-y}Co\text{-}Mn_yO_2$ lattice at deep charge irrespective of nickel content in lithium-ion batteries. *J Am Chem Soc* 2019; **141**: 5097-101.
23 You Y, Celio H and Li J *et al.* Modified high-nickel cathodes with stable surface chemistry against ambient air for lithium-ion batteries. *Angew Chem Int Ed* 2018; **57**: 6480-5.
24 Kalluri S, Yoon M and Jo M *et al.* Feasibility of cathode surface coating technology for high-energy lithium-ion and beyond-lithium-ion batteries. *Adv Mater* 2017; **29**: 1605807.
25 Li W, Dolocan A and Oh P *et al.* Dynamic behaviour of interphases and its

implication on high-energy-density cathode materials in lithium-ion batteries. *Nat Commun* 2017; **8**: 14589.

26 Kong F, Liang C and Wang L *et al.* Kinetic stability of bulk $LiNiO_2$ and surface degradation by oxygen evolution in $LiNiO_2$-based cathode materials. *Adv Energy Mater* 2019; **9**: 1802586.

27 Bi Y, Tao J and Wu Y *et al.* Reversible planar gliding and microcracking in a single-crystalline Ni-rich cathode. *Science* 2020; **370**: 1313-7.

28 Denton AR and Ashcroft NW. Vegard's law. *Phys Rev A* 1991; **43**: 3161-4.

29 Nicholas JD and De Jonghe LC. Prediction and evaluation of sintering aids for cerium gadolinium oxide. *Solid State Ion.* 2007; **178**: 1187-94.

30 Accardo G, Frattini D and Ham HC *et al.* Direct addition of lithium and cobalt precursors to $Ce_{0.8}Gd_{0.2}O_{1.95}$ electrolytes to improve microstructural and electrochemical properties in IT-SOFC at lower sintering temperature. *Ceram Int* 2019; **45**: 9348-58.

31 Kim, Y., Lee, H. and Kang, S. First-principles and experimental investigation of the morphology of layer-structured $LiNiO_2$ and $LiCoO_2$. *J Mater Chem* 2012; **22**: 12874-81.

32 Jung SK, Hwang I and Chang D *et al.* Nanoscale Phenomena in lithium-ion batteries. *Chem Rev* 2020; **120**: 6684-737.

33 Manthiram A. A reflection on lithium-ion battery cathode chemistry. *Nat Commun* 2020; **11**: 1550.

34 Winter M, Barnett B and Xu K. Before Li-ion batteries. *Chem Rev* 2018; **118**: 11433-56.

35 Schmuch R, Wagner R and Hörpel G *et al.* Performance and cost of materials for lithium-based rechargeable automotive batteries. *Nat Energy* 2018; **3**: 267-78.

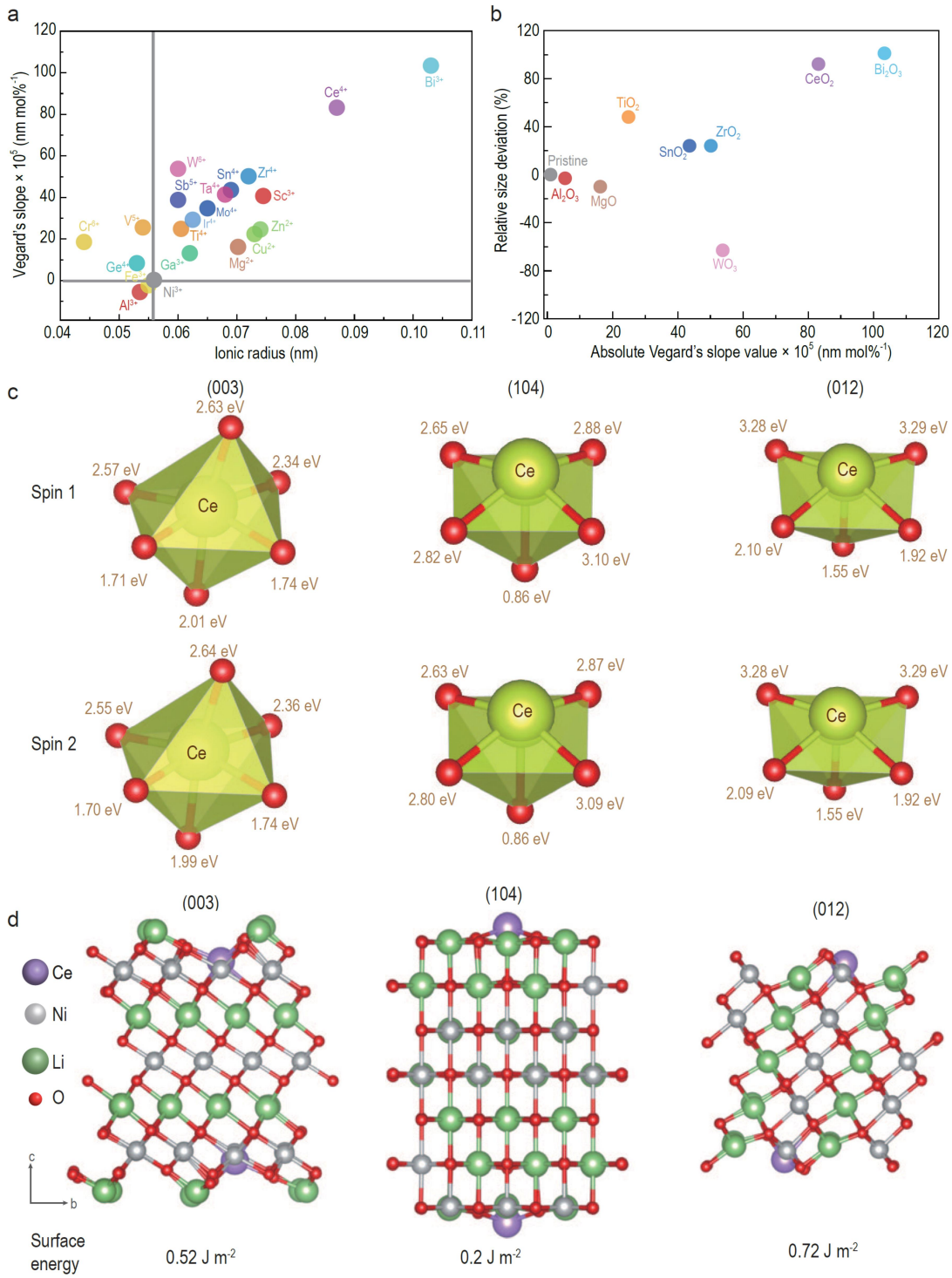

Figure 1. Sintering aids effect on the crystal growth. (a) Vegard's Slope vs ionic radius for possible sintering aids. (b) The relative particle size deviation of SCNR materials synthesized with different sintering aids compared with the pristine NCM materials. The size deviation is the size difference between the cathodes calcined with varied sintering aids and the bare cathode. (c) The bond strength between surface transition metal Ce and oxygen atoms, obtained by crystal orbital Hamilton

population (COHP) analysis. (d) The surface energy of typical exposed facets in Ni-rich cathode materials (003), (104) and (012) after the introduction of Ce^{4+}.

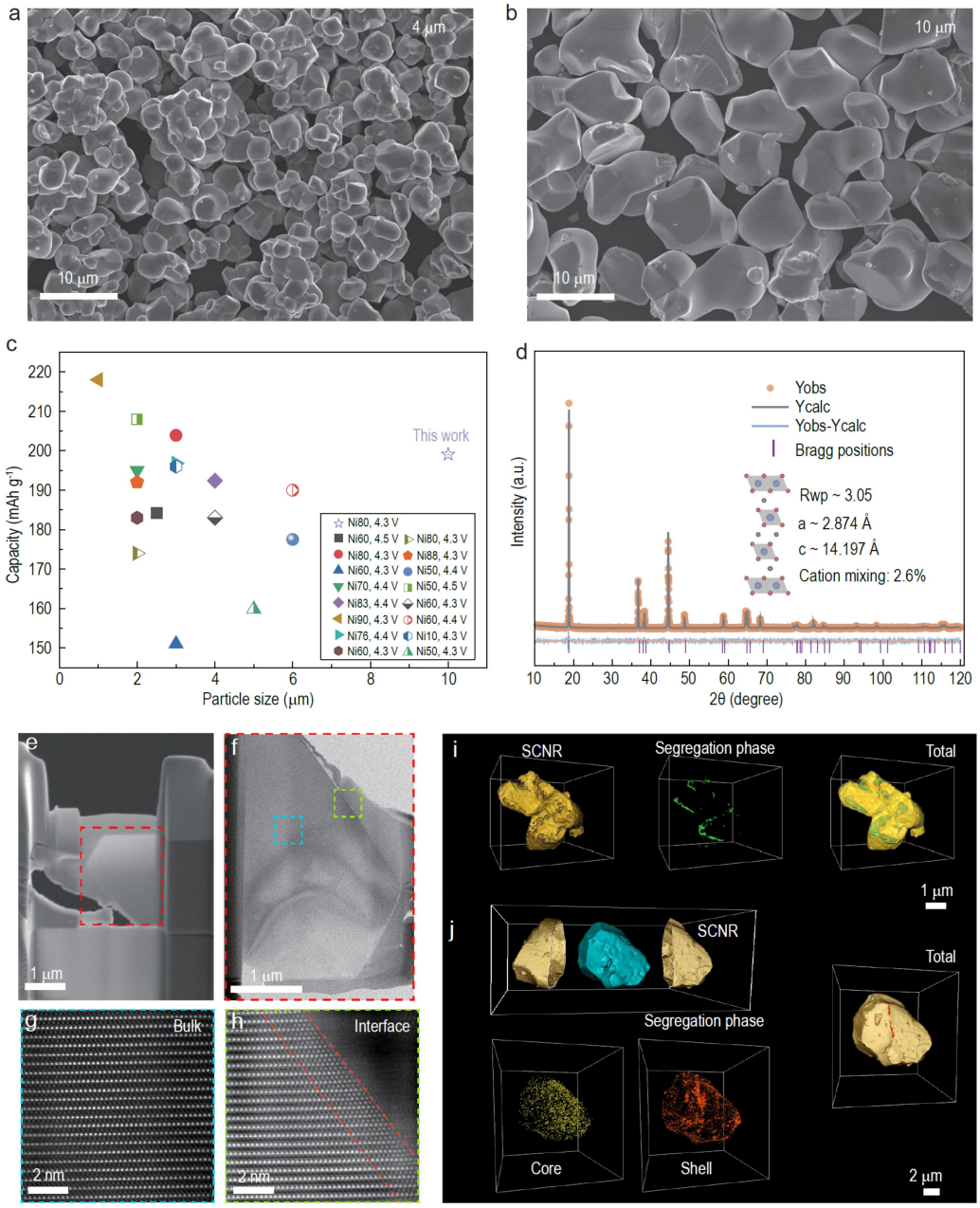

Figure 2. The morphology, structure and phase distribution of SCNR cathodes. SEM images of SCNR materials with the particle size of 4 μm (a) and 10 μm (b) and the scale bars are10 μm. (c) Particle size and capacity comparison of SCNR cathode from this work and high capacity single-crystalline NCM cathodes from the literature. (d) Rietveld refinement of SCNR cathode with particle size of 10 μm. (e and f) SEM image and low-magnified STEM image of SCNR cathode sample prepared by FIB. (g and h) High-resolution STEM images of SCNR cathode. (i and j) 3D spatial distribution of different phases in SCNR particles, probed by Nano-CT.

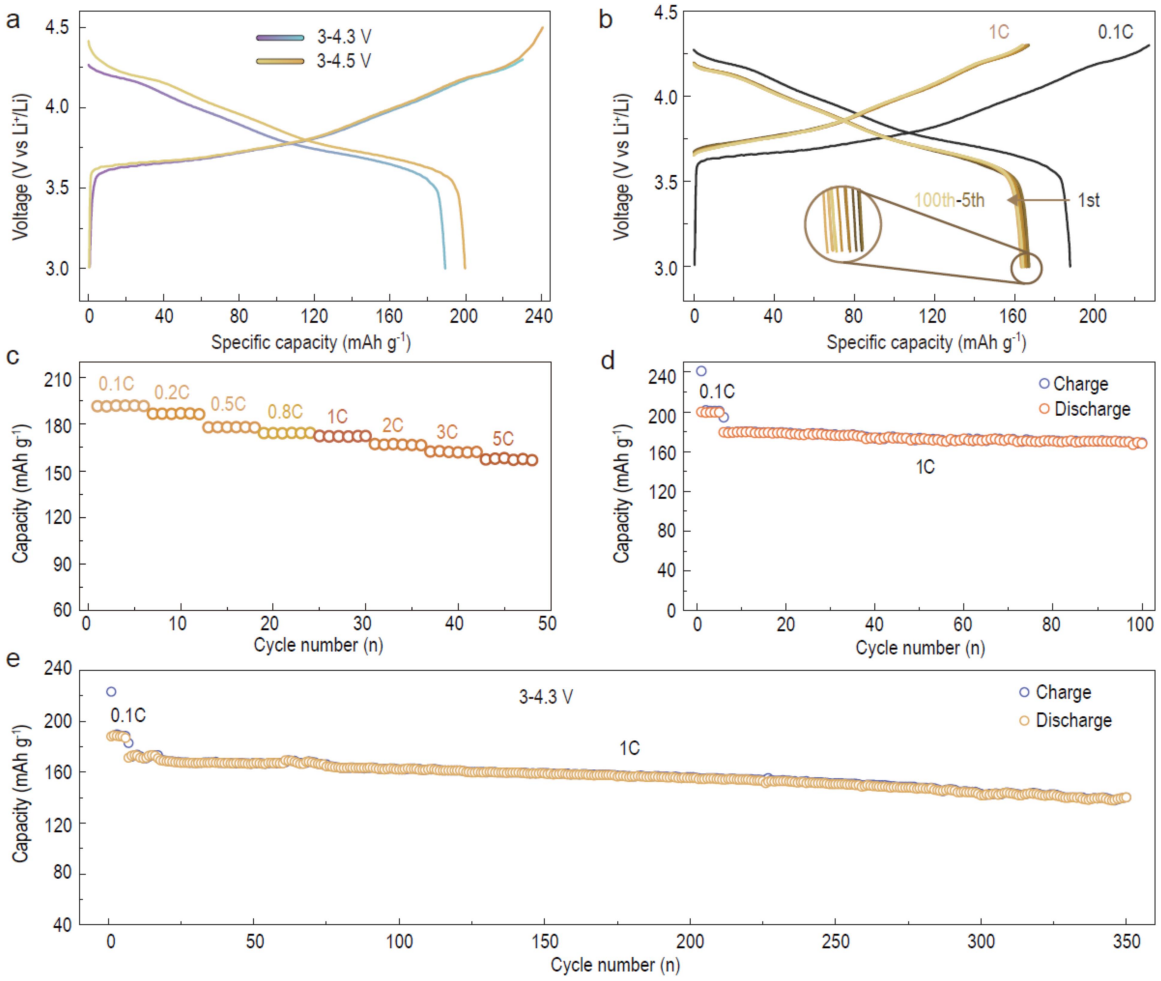

Figure 3. Electrochemical performances of SCNR cathodes with the particle size of 10 μm in coin-cells. (a) The 1st charge-discharge curves of the SCNR half-cell at the charge cut-off voltages of 4.3 and 4.5 V. (b) The charge-discharge curves of the SCNR half-cell for the first 100 cycles. For the first 5 cycles, the cell was tested at 0.1C, and then at 1C for the subsequent cycles. (c) Rate performances of the SCNR half-cell. The charge and discharge rate before 1C is the same, and the charge rate is 1C with discharge rate varying from 1C to 5C. (d and e) Cycle performances of the SCNR cells at the charge cut-off voltages of 4.5 and 4.3 V.

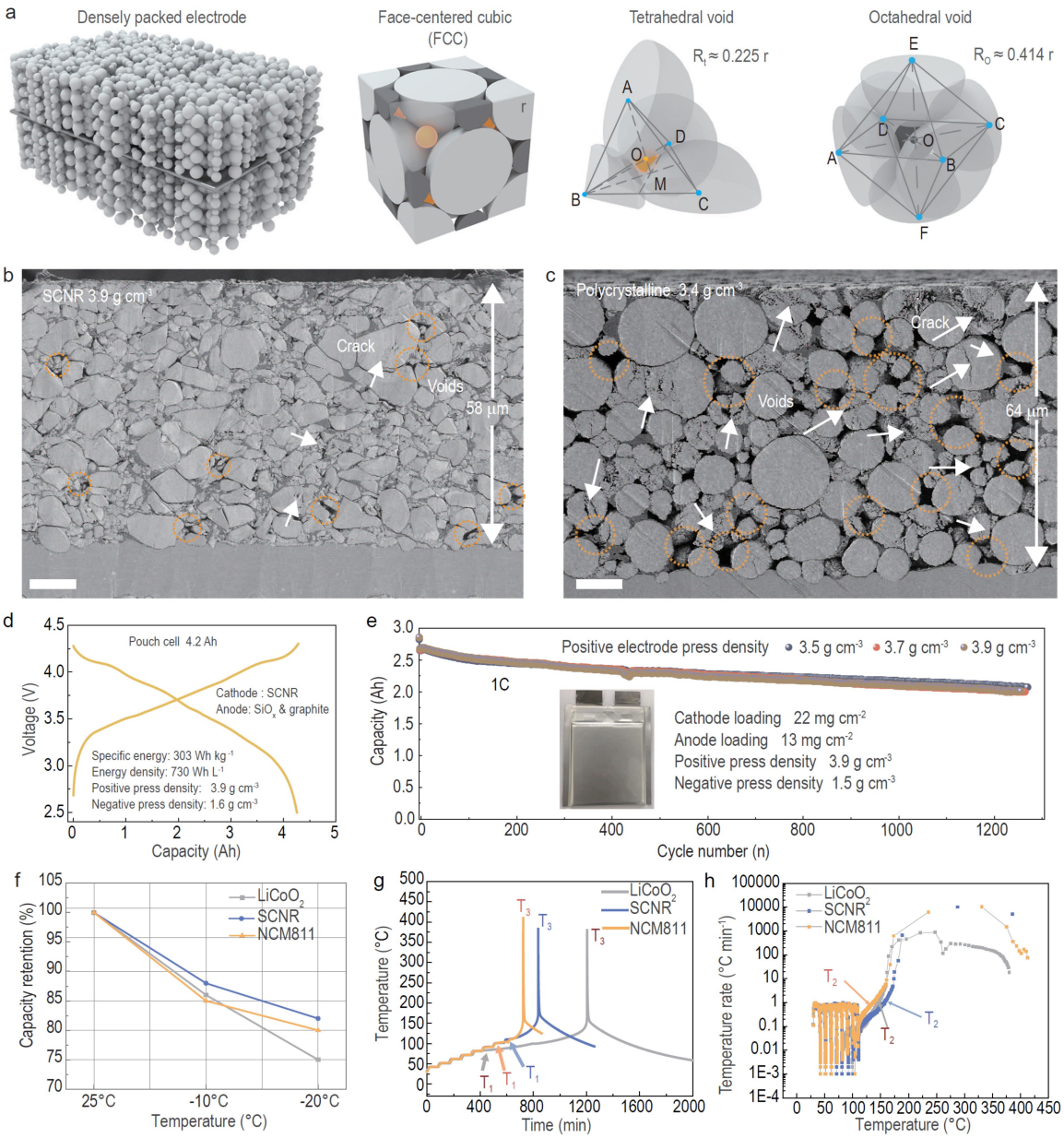

Figure 4. Characterizations of the SCNR material under practical application conditions. (a) Schematic illustration of the dense electrode and four octahedral voids and eight tetrahedral voids in each unit cell. (b and c) The cross-section SEM images of SCNR and polycrystalline spherical NCM811 electrodes with the same capacity of 4.5 mAh cm^{-2}. The Scale bars are 10 μm. (d) Charge and discharge curve of SCNR|SiO_x&graphite pouch cell. (e) Cycle performances of SCNR|graphite pouch cells. (f) The comparison of the $LiCoO_2$, SCNR and polycrystalline spherical NCM811 cathodes in pouch cells under low temperature. (g and h) The comparison of T-t curve and temperature rates of the $LiCoO_2$, SCNR and polycrystalline spherical NCM811 cathodes in pouch cells.

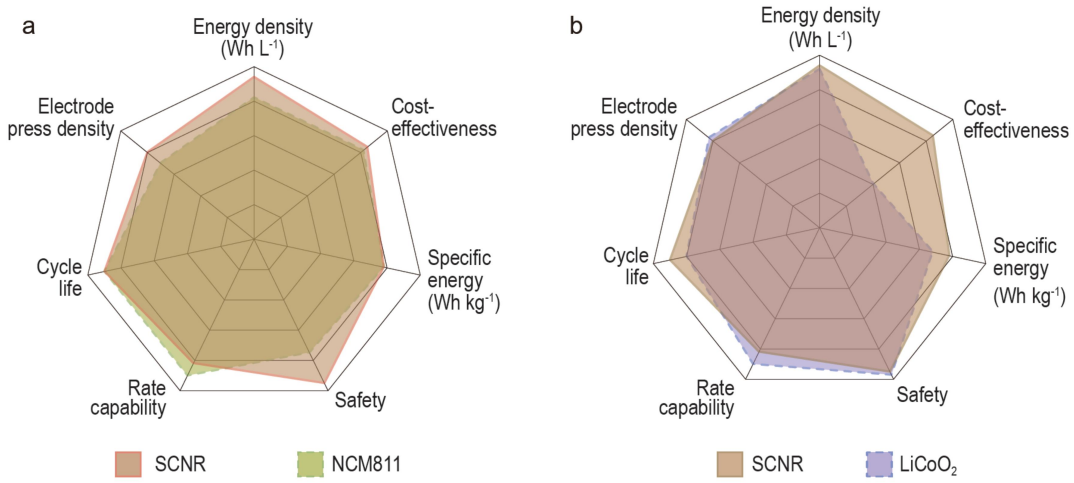

Figure 5. Benchmarking SCNR cathodes against polycrystalline spherical NCM811 (a) and $LiCoO_2$ (b). The Radar maps comparing the SCNR cathode with polycrystalline NCM811 and $LiCoO_2$ in terms of several key parameters that are critical for practical applications.